Applied Surface Science 579 (2022) 152146

Contents lists available at ScienceDirect

Applied Surface Science

journal homepage: www.elsevier.com/locate/apsusc

Full Length Article

Transition metal (Nb and W) doped TiO_2 nanostructures: The role of metal doping in their photocatalytic activity and ozone gas-sensing performance

Emerson Santos [a], Ariadne C. Catto [a,b], Allan F. Peterline [a], Waldir Avansi Jr [a,b,*]

[a] Laboratory of Nanostructured Multifunctional Materials, Department of Physics, Federal University of São Carlos, UFSCar, São Carlos 13565-905, Brazil
[b] Center for the Development of Functional Materials (CDMF), Federal University of São Carlos, São Carlos, SP 13565-905, Brazil

ARTICLE INFO

Keywords:
Hydrothermal treatment
TiO_2 nanostructures
Gas sensor
Photocatalytic activity

ABSTRACT

Semiconducting metal oxide nanostructures have drawn much attention from the researchers due to several advantages related to their wide-ranging applications, such as photocatalytic activity and gas-sensing performance. In this way, the effect of metal ions on the structural, morphological and electronic properties of the as-prepared samples were investigated by X-ray diffraction (XRD), Raman spectroscopy, UV–visible diffuse reflectance spectra (DRS), X-ray photoelectron spectroscopy (XPS) and electron microscopy techniques. XRD analysis confirmed that all $M_xTi_{1-x}O_2$ (M = Nb and W) samples presented only the TiO_2 anatase phase despite the different amounts of dopant. Additionally, scanning electron microscopy (SEM) showed that the increased metal ion content leads to a morphological evolution from anisotropic to isotropic nanostructures, which consequently reduces their size. It was observed that the presence of W and Nb as dopants clearly induces a change in the surface characteristics of the nanostructures, favoring the photodegradation of cationic dyes, which does not occur for Rhodamine (RhB) since the photocatalytic mechanism appears strictly related to carrier charges. From the studied samples, $W_{0.29}Ti_{0.71}O_2$ presented interesting ozone (O_3) gas-sensing performance, which was evidenced by their working temperature (below 150 °C), sensor response, stability and good range of detection.

1. Introduction

The need for a healthier ecosystem makes the development of new materials one of the main challenges of applied physics, chemistry and materials science. In this way, the development of nanostructured semiconductors with improved technological performance appears as an important research area. Among them, we can highlight titanium dioxide (TiO_2), which has been considered one of the most important multifunctional materials, especially in anatase crystalline phase, being extensively investigated due to its wide range of applications [1–16]. In fact, considerable efforts have been devoted to improving the properties of such materials, especially through band-gap engineering, allowing their application in technological devices, e.g., photocatalysis and chemiresistive sensors [1–24]. Thus, the use of transition metals as dopants, such as vanadium (V), tungsten (W), iron (Fe), niobium (Nb) and so on, appears as a promising strategy to improve the performance of photocatalysis or chemiresistive sensors [1–23] On the other hand, the doping mechanism of metal ions in TiO_2 structures and their structural and electronic effects, such as the type and different concentrations of dopant ions, still attracts the interest of many researchers.

The main aspects attributed to modifications induced by doping could be related to a band-gap reduction, leading to an enhanced separation of electron-hole pairs, changes in morphology and electronic structures [1,2,4–8,12,19–24]. The improvement of the TiO_2 properties due to the effect of presence of dopants have been associated with the introduction of defects in its lattice, creating additional energy levels located between bands, and even inhibiting the anatase-to-rutile transformation [1,2,4–8,12,19–24]. As a consequence, during the procedures to obtain the nanostructures one often encounters the challenging need to precisely control the concentration and location of dopants in a host system [2,4,8–11,18,22,25,24,26,27], providing a better understanding on the application of such materials [4,8,10,11]. Despite the fact that several strategies have been employed to improve the properties of doped TiO_2, the effect of these strategies could be negative depending on the location of the dopant [4,8,10,11]. For instance, Kang et al. reported that the photocatalytic performance of metal doped TiO_2 is not remarkably due to the presence of metal on the TiO_2 surface, which can block reaction sites [24]. Chang et al. studied the effect of different types

* Corresponding author.
E-mail address: w_avansi@ufscar.br (W. Avansi Jr).

https://doi.org/10.1016/j.apsusc.2021.152146
Received 11 October 2021; Received in revised form 30 November 2021; Accepted 4 December 2021
Available online 8 December 2021

of transition metal ions in the TiO_2 surface lattice on its photocatalytic performance. According to this study, doped Fe, Cu and V ions improve the photocatalytic activity, whereas Mn, Ce and W ions cause adverse results [4]. Indeed, the distribution, presence and stability of oxygen (O) vacancies induced by the dopant element in oxide nanomaterials also needs to be further explored in order to control the desired effects [4,8,10–12,24]. In a previous work, we reported a detailed study on the synthesis of $V_xTi_{1-x}O_2$ nanostructures obtained by a simple and environmentally-friendly hydrothermal method at low temperature and short synthesis time [22]. Additionally, a morphological evolution from anisotropic to isotropic nanostructures was observed as a function of the V content, where XANES at V K edge and atomic-resolved EELS measurements revealed that the vanadium ions preferentially occupy Ti^{4+} sites distributed in the particle without any segregation [22].

Concerning the application of TiO_2 as a gas-sensing layer, there are relatively few reports in the literature, mainly because TiO_2 is an n-type semiconductor with high resistance and poor conductivity, which greatly affects its gas-sensing performance [1]. In this regard, the addition of metal ion appears as an interesting alternative to improve and extend the technological applications of anatase TiO_2 as a gas-sensing layer [1,8,10]. Epifani et al. studied the use of anatase TiO_2 nanocrystals obtained by solvothermal process in the presence of W and their gas-sensing properties towards ethanol vapor. They showed that the surface modification of the TiO_2 host due to the presence of WO_3 nanocrystal enhanced the sensor response in 3 orders of magnitude compared to pure TiO_2 [10]. In a second study, Epifani et al. also showed that the deposition of V species on the surface of anatase TiO_2 nanocrystals resulted in an improvement of the sensor response up to almost 2 orders of magnitude compared to pure TiO_2, clearly evidencing the catalytic effect of V addition [8].

Despite the fact that nanostructured semiconductors have demonstrated various advantages related to their gas-sensing performance towards reducing and oxidizing gases, ozone (O_3) has attracted a special attention, as it is considered an air pollutant with several adverse effects to human health, being commonly associated with morbidities and mortality [28–32]. As a matter of fact, many sensor devices based on semiconductor oxides, such as V_2O_5/TiO_2 [13], WO_3 [33,34], SnO_2 [35], ZnO [28], Ag_2WO_4 [36] and $CuWO_4$ [37], have been studied towards O_3 gas. In a recent study, our group investigated the effect of cobalt addition on the ozone gas-sensing properties of nanostructured ZnO thin films. We observed an enhanced sensor response as a function of Co content, which was linked to the catalytic activity provided by Co ions in the semiconductor oxide and the presence of oxygen vacancies on the semiconductor oxide surface [28]. However, advances are still lacking regarding their working temperature, region of operation (concentration) and response and recovery times.

Therefore, the aim of this work is to provide a detailed investigation on the preparation of $M_xTi_{1-x}O_2$ (M = Nb and W) nanostructures by hydrothermal treatment of peroxo-metal complex, which is considered to be a simple and environmentally-friendly methodology. Additionally, a combination of spectroscopic techniques, such as Raman, X-ray photoelectron spectroscopy (XPS) and UV–visible diffuse reflectance spectra (DRS), and electron microscopy techniques was then performed to provide comprehensive information about the structural and electronic characteristics of such materials correlated with their photocatalytic activity and ozone gas-sensing performance.

2. Materials and methods

2.1. Synthesis of materials

The oxidant peroxide method (OPM) with crystallization under hydrothermal conditions has great potential to synthesize nanostructured oxide semiconductors to be applied as photocatalysts or chemiresistors, especially for being a simple methodology that uses low temperatures and no additives [38]. The $M_xTi_{1-x}O_2$ (M = W and Nb) samples were obtained through the simultaneous decomposition of peroxo metal complex by hydrothermal treatment, in a similar procedure already reported by our group [14,22,39,40]. In the first step, the peroxo titanium complex was obtained according to the procedure described by Ribeiro et al.[41], where a specific amount of metallic Ti (99.7%, Aldrich) was added into 80 mL of H_2O_2/NH_3 solution (both 29.0%, Synth). Peroxo tungsten (W) and niobium (Nb) complexes were prepared by dissolving Tungstic Acid (H_2WO_4, Aldrich) and Ammonium Niobium Oxalate ($NH_4[NbO(C_2O_4)_2(H_2O)_2]\cdot nH_2O$, CBMM) in an H_2O_2 solution, as described by de Castro et al. [14] and Lopes et al. [17], respectively. Then, an appropriate amount of the complex solutions were mixed in order to obtain $M_xTi_{1-x}O_2$ (M = W and Nb) samples with desired metal ion content, submitting the solution to a hydrothermal cell. The studied amounts of the above mentioned metal ions (x atom %) were determined by energy-dispersive X-ray spectroscopy (EDS). The synthesis conditions for all samples were set at 200 °C for 6 h. The as-synthesized samples were centrifuged, washed several times with distillated water and isopropanol, and dried at 60 °C for 8 h.

2.2. Characterization

The $M_xTi_{1-x}O_2$ (M = W and Nb) samples were investigated by X-ray diffraction (XRD) using a Shimadzu XRD 6100 diffractometer with Cu k_α ($\lambda = 1.5406$Å) radiation and a monochromator in continuous mode at a scan step of 0.02° and exposure time of 1 s.

Raman measurements were performed at room temperature using an FT-Raman instrument (Brucker RAM II) equipped with a Ge detector and an Nd-YAG laser, operating at 1064 nm and a maximum power of 100 mW. The spectra were recorded from 100 to 800 cm^{-1}.

The specific surface area (SSA) measurements were carried out at liquid nitrogen temperature by applying the single-point BET method, monitored from the nitrogen adsorption-desorption isotherms measured at 77 K on a Micromeritics ASAP 2420 A (USA) surface area and porosimetry analyzer.

The sizes and morphologies of the samples were determined by field emission scanning electron microscopy (FE-SEM) using JEOL JSM6701F and Zeiss VP Supra 35 microscopes. The as-obtained samples were also studied by transmission electron microscopy (TEM). Conventional TEM and high-resolution (HRTEM) studies were performed on a JEM 2100F URP operating at 200 KV. Additionally, the chemical analyses of the samples were performed by energy-dispersive X-ray spectroscopy (EDS) using an EDS Thermo-Noran microanalysis system equipped with a Si detector attached to the JEOL JSM 6510 and Oxford SDD 100 mm^2 microanalysis attached to the JEOL 2100F microscope.

In order to analyze the effect of optical properties of metal ions (Nb or W) on TiO_2 materials, UV–visible diffuse reflectance spectra (DRS) were acquired through a Shimadzu UV2600 in the 250–800 nm range. The as-obtained spectra were converted using the Kubelka-Munk function [42] and normalized. The band-gap of the samples was calculated according to the equation proposed by Tauc et al. [43]

The XPS analysis was performed on a Thermo Scientific K-Alpha spectrometer using a monochromatic Al Kα source. The data were analyzed using Casa XPS software (Casa Software Ltda., U.K.), and the spectra were calibrated using a C 1 s line (284.8 eV) of the adsorbed C on the sample surface.

2.3. Photocatalytic activity

The photocatalytic performance of the studied samples was evaluated through the procedures already reported by our group [21,44,45]. The photocatalytic activity of the $M_xTi_{1-x}O_2$ (M = W and Nb) samples was tested for the degradation of Rhodamine B (RhB) and Methylene Blue (MB) dyes (Aldrich 95%) in aqueous solutions under ultraviolet (UV) light irradiation. In this procedure, an amount of 10 mg of the $M_xTi_{1-x}O_2$ (M = W and Nb) samples was dispersed in 30 mL of RhB (5 mg/L) and MB (10 mg/L) solutions, which were subsequently illuminated by six lamps (Philips TL-D, 15 W) in a photocatalytic system maintained at room temperature (25 °C) in a thermostatic bath under vigorous stirring. Aliquots were collected at fixed time intervals (0, 15, 30 and 45 min). Variations in the absorption band maximum at $\lambda = 553$ nm (RhB) and 664 nm (MB) were measured by performing UV–Vis absorption spectroscopy measurements of the solution on a Shimadzu UV2600 spectrophotometer.

2.4. Preparation of the sensing platforms and gas-sensing measurements

To perform the gas-sensing measurements, we adopted a typical procedure used by our group [13,36,37]. In the first step, the pure TiO_2 and $M_xTi_{1-x}O_2$ (M = W e Nb) samples were dispersed in isopropyl alcohol in an ultrasonic cleaner for 30 min, and the suspension was then dripped onto a SiO_2/Si substrate with interdigitated Pt electrode arrays with thicknesses of 100 nm and spaced 50 μm apart. Subsequently, the samples were annealed for another 30 min at 500 °C in an electric oven under air atmosphere.

The sensor samples were inserted into a specific chamber to allow dynamic gas-sensing measurements. Available in our lab [13], this workbench provides the control of the substrate temperature and ozone concentration. Ozone gas was formed from oxidizing oxygen molecules of dry air using a calibrated pen-ray UV lamp (UVP, model P/N 90–0004-01), providing a concentration range of 12 to 94 ppb (parts-per-billion). The ozone levels were calibrated by a toxic gas detector (ATI, model F12). The total gas flow rate was kept constant and equal to 500 SCCM by using a mass flow controller (MFC). The O_3 levels were calibrated by the same toxic gas detector. The sensor response was $S = R_{air}/R_{O3}$, where R_{air} and R_{O3} are the electric resistances of the device exposed to dry air and gas, respectively. In addition, the response and recovery times were defined as the time required for the resistance to reach 90% of its initial value when exposed to the target gas and after the detected gas is turned off, respectively [13]. To determine the long-term stability over 1 year, the sample was stored and exposed to 20 ppb of ozone gas at a working temperature of 100 °C every day, and the repeated adsorption/desorption cycles were measured.

3. Results and discussion

Fig. 1 shows the XRD patterns of the as-obtained $M_xTi_{1-x}O_2$ (M = W and Nb) samples, where it is possible to confirm that all diffraction peaks can be attributed to the TiO_2 anatase phase, according to the Joint Committee on Powder Diffraction Standards (JCPDS 21–1272). Indeed, for both $W_xTi_{1-x}O_2$ (Fig. 1a) and $Nb_xTi_{1-x}O_2$ (Fig. 1b) samples, only peaks corresponding to the (101), (103), (004), (112), (200), (105) and (211) planes were observed at around 25.3°, 36.9°, 37.8°, 38.4°, 47.8°, 53.8° and 54.7°, respectively.

The Raman spectroscopy technique was employed to study the presence of defects and the nanoparticle size of the TiO_2 nanostructures [6,8,12,23,26,46]. Fig. 2 displays the Raman spectra obtained for the

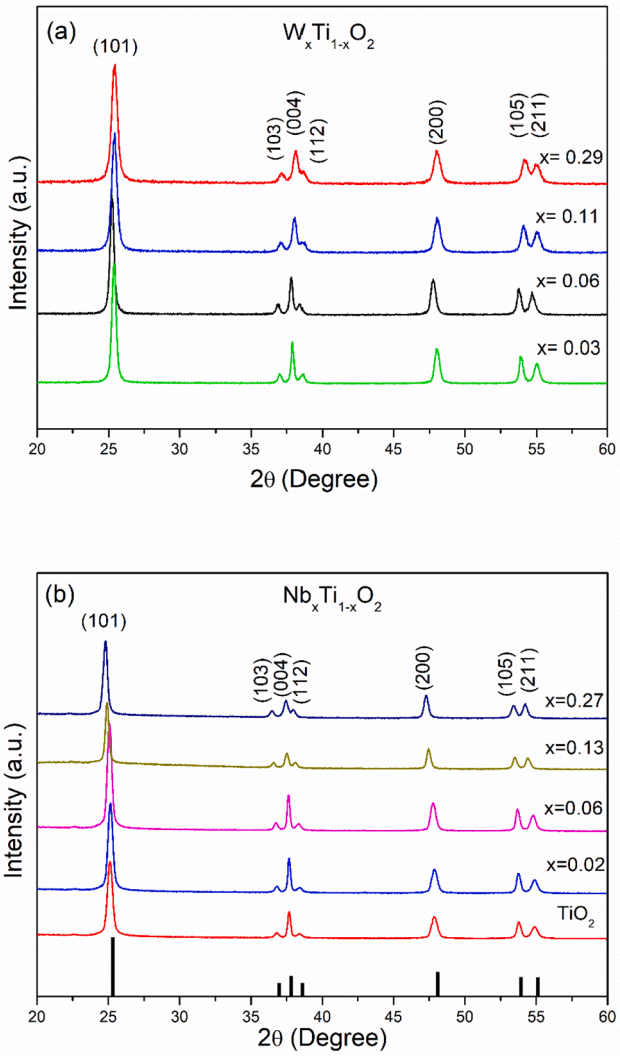

Fig. 1. XRD patterns of the as-synthesized $M_xTi_{1-x}O_2$ (M = W and Nb) samples: (a) $W_xTi_{1-x}O_2$ and (b) $Nb_xTi_{1-x}O_2$. The observed reflections correspond to the TiO_2 anatase phase (JCPDS file #21–1272).

$M_xTi_{1-x}O_2$ (M = W and Nb) samples, where a typical spectrum for the anatase phase of the TiO_2 compound can be seen, revealing good agreement with the XRD measurements. The typical Raman-active modes of TiO_2 anatase were observed at around 147 cm^{-1} (E_g), 199 cm^{-1}(B_{1g}), 399 cm^{-1} (B_{1g}), 517 cm^{-1} ($A_{1g} + B_{1g}$) and 637 cm^{-1} (E_g) for all studied samples [6,8,12]. On the other hand, from the analysis of an expanded view of region 100–250 cm^{-1} (Fig. 2b and d) it is clear that the presence of metal ions (more specifically Nb and W) caused a shift towards higher wavenumbers for the E_g mode, with a consequent broadening of this peak around 5 cm^{-1}. This behavior was previously reported in the literature and attributed to the presence of oxygen vacancies [12] or crystallite size [46]. In fact, the displacement and broadening of the E_g peak changed with the increase of dopant (Nb and W) content. Gardecka et al. also observed this effect, emphasizing that the crystal lattice changes due to the effective doping of Nb^{+5} and W^{+4} in the TiO_2 host structure [26]. Furthermore, the increase in the Nb doping level of the B_{1g} peak from 2% to 27% led to significant frequency shifts to lower

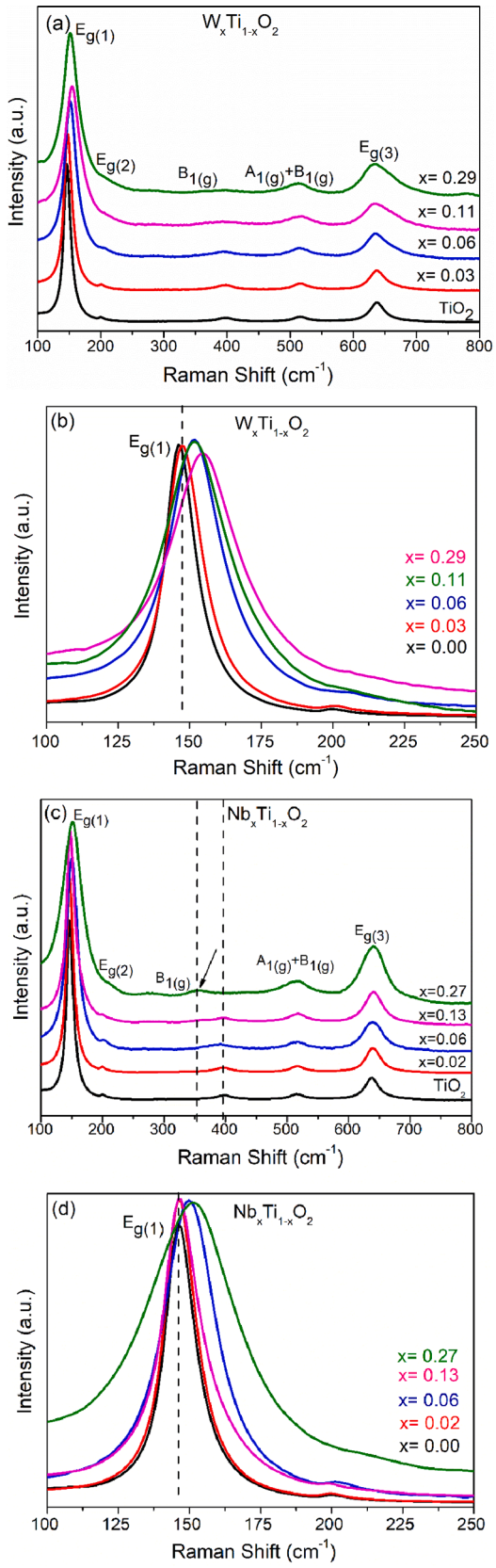

Fig. 2. Raman spectra of $M_xTi_{1-x}O_2$ (M = W and Nb) samples: (a-b) $W_xTi_{1-x}O_2$ and (c-d) $Nb_xTi_{1-x}O_2$.

wavenumbers. These changes can be related to the increased average distance between ions as a result of Ti^{+4} vacancies after Nb^{+5} doping and the formation of Nb-O-Ti bonds [23].

The morphology of the samples doped with W and Nb ions was also studied by SEM (Fig. 3). From the representative images, it was possible to verify a direct influence of both ions on the morphological evolution of the studied nanostructures depending on their nature or even their quantity, as observed in a previous work [22]. Indeed, regardless of the metal ion content, it was noted that the different amounts of dopant led to the formation of isotropic nanostructures with reduced size dimensions, approximately equal to (14.8 ± 0.2) and (23.9 ± 0.4) nm for $Nb_{0.27}Ti_{0.73}O_2$ and $W_{0.29}Ti_{0.71}O_2$, respectively. Moreover, it was possible to observe a homogeneous distribution in the dimensions and shapes of the obtained nanostructures. It is important to highlight that according to the SEM images and XRD analysis, the difference observed in the Raman results is possibly related to the appearance of network defects induced by the presence of ions in the crystal lattice.

Chemical mapping analyses using the energy-dispersive X-ray energy spectroscopy (EDS) technique confirmed the presence of only W, Ti and O atoms for the $W_{0.29}Ti_{0.71}O_2$ samples and Nb, Ti and O atoms for the $Nb_{0.27}Ti_{0.73}O_2$ samples. The EDS measurements also pointed to a homogeneous distribution of the doping elements, as shown in Fig. 4a and 4b, confirming the efficiency of the synthesis methodology used herein.

In addition, the HRTEM images (Fig. 5) and their respective fast Fourier transforms (FFT) of the nanostructures showed that even for the largest amount of dopant, the $M_xTi_{1-x}O_2$ samples (M = W and Nb) obtained were monocrystalline in nature, with no evidence of segregation of the doping material, as previously observed for the $V_xTi_{1-x}O_2$ samples [22], indicating the success of the proposed procedure for obtaining TiO_2 anatase phase nanostructures containing Nb and W metal ions.

The morphological and compositional changes as a result of the addition of W or Nb led to modifications of the optical properties of the TiO_2 nanostructures, causing a slight change in the optical absorption band, as observed for the $M_xTi_{1-x}O_2$ samples (M = W or Nb) (Fig. 6a). As no significant difference was noted between the different amounts of dopant, we presented herein only the results related to the highest amount in comparison with the undoped sample (pure TiO_2). Fig. 6b illustrates the absorption spectrum obtained through the Kubelka-Munk equation, where it is possible to observe values for the forbidden band energy around 3.2 and 3.1 eV for $Nb_{0.27}Ti_{0.73}O_2$ and $W_{0.29}Ti_{0.71}O_2$ samples, respectively. Even though the values obtained for the TiO_2 samples are within the expected for the anatase phase, there was a significant difference when compared to the $V_xTi_{1-x}O_2$ samples obtained by a similar synthesis methodology [22]. In contrast, there was no significant variation between the $Nb_{0.27}Ti_{0.73}O_2$ and $W_{0.29}Ti_{0.71}O_2$ samples. However, it is worth mentioning that these analyses did not show a sufficient bandwidth energy shift from the ultraviolet (UV) to the visible region of the electromagnetic spectrum [22].

As our purpose was to evaluate the photocatalytic performance and gas-sensing properties of $M_xTi_{1-x}O_2$ (M = W or Nb) samples, whose performance could be related to surface properties, theses samples were also analyzed by the XPS technique. Fig. 7a and b show the high-resolution (HR) W 4f XPS spectrum of the $W_{0.03}Ti_{0.97}O_2$ and $W_{0.29}Ti_{0.71}O_2$ samples. The spectra were deconvoluted considering multiple contributions of six components: two peaks at 37.0 and 39.7 eV, corresponding to Ti 3p and W 5p 3/2, respectively, and four peaks from the W 4f spin–orbit doublet (4f 7/2 and 4f 5/2), with binding energy (BE) values at 35.5 and 37.6 eV attributed to the presence of W^{+6} atoms, and at 34.2 and 36.3 eV due to the contribution of the W^{5+} states [4,7,10,47,48]. Thus, the XPS results revealed the presence of W^{m+} species, evidencing that the W^{6+}/W^{5+} ratio increases with the doping concentration from 3.6 to 6.7 for the $W_{0.03}Ti_{0.97}O_2$ and $W_{0.29}Ti_{0.71}O_2$ samples, respectively, thus indicating the higher amount of W^{6+} ions for the $W_{0.29}Ti_{0.73}O_2$ sample.

Fig. 8a and b display the HR Nb 3d XPS spectra of the $Nb_{0.02}Ti_{0.98}O_2$ and $Nb_{0.27}Ti_{0.73}O_2$ samples, confirming the presence of spin–orbit

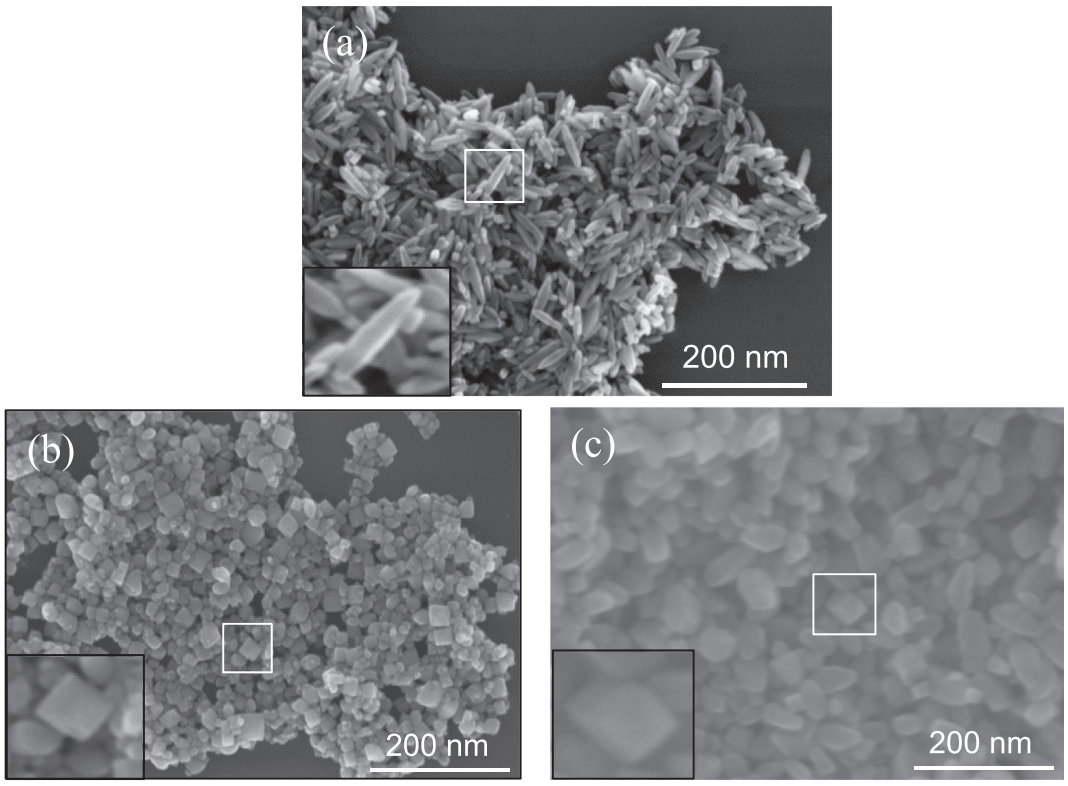

Fig. 3. SEM images of the as-synthesized $M_xTi_{1-x}O_2$ (M = W and Nb) samples: (a) TiO_2, (b) $Nb_{0.27}Ti_{0.73}O_2$ and (c) $W_{0.29}Ti_{0.71}O_2$.

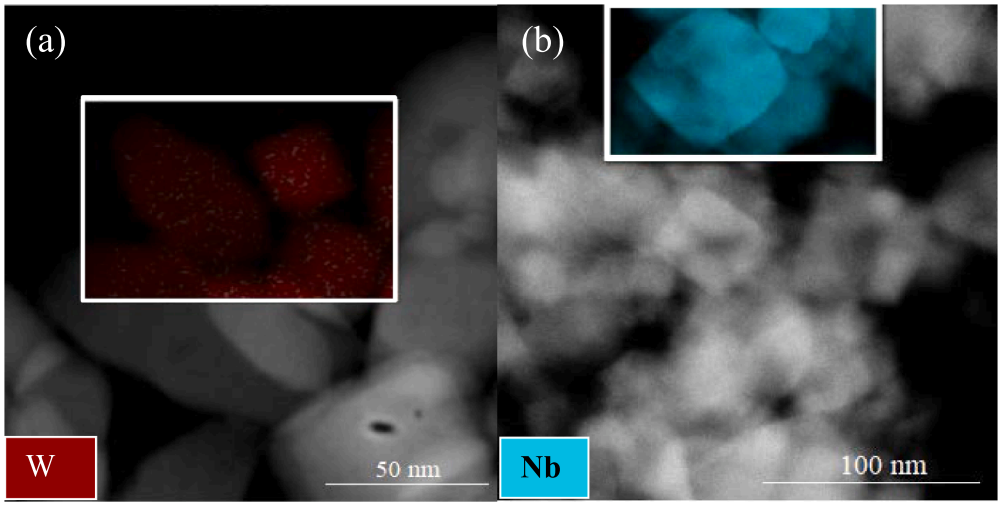

Fig. 4. HAADF-STEM images of the (a) $W_{0.29}Ti_{0.71}O_2$ and (b) $Nb_{0.27}Ti_{0.73}O_2$ samples. In the inset: their respective distribution of the W (red) and Nb (blue) chemical elements illustrated by the overlapping image due to the presence of the elements.

doublet corresponding to Nb $3d_{3/2}$at 207.8 eV and Nb $3d_{5/2}$ at 210.6 eV and related to the oxidation state of Nb^{5+} [3,23].

Fig. 9 shows the HR Ti 2p XPS spectra for the TiO_2, $Nb_{0.02}Ti_{0.98}O_2$, $Nb_{0.27}Ti_{0.73}O_2$, $W_{0.03}Ti_{0.97}O_2$ and $W_{0.29}Ti_{0.71}O_2$ samples, revealing Ti $2p_{3/2}$ and Ti $2p_{1/2}$ peaks centered at 458.8 and 464.4 eV, respectively, which is in good agreement with previous studies [3]. A detailed analysis of the Ti 2p spin-orbit doublet revealed the contribution of four components pointing to the occurrence of the Ti ion in different oxidation states, being the Ti $2p_{3/2}$ and Ti $2p_{1/2}$ peaks located at 457.4 and 463.2 eV, respectively, assigned to the presence of Ti^{+3} atoms, while the main components at 459.0 and 464.8 eV were attributed to the presence of Ti^{+4} atoms [3].

The relative Ti^{+3}/Ti^{+4} atomic percentages of the studied samples were calculated in relation to the ratio of each area of the respective

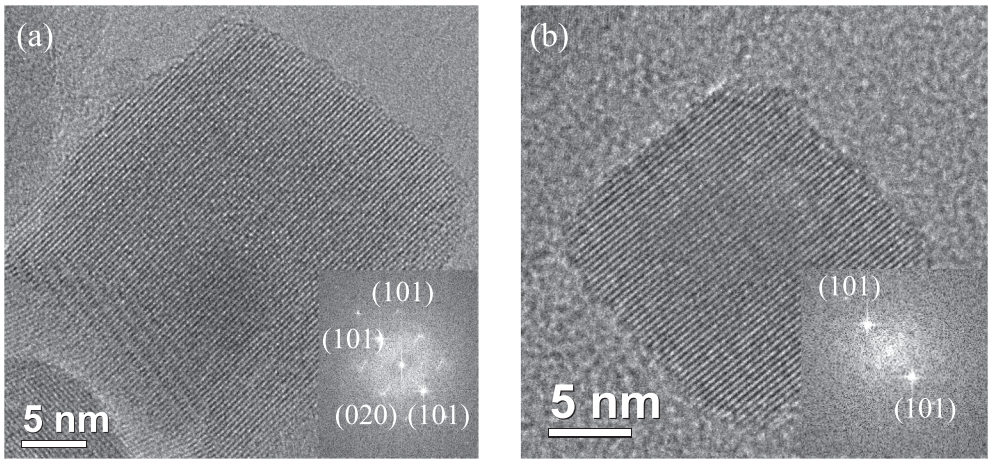

Fig. 5. HRTEM images of the $M_xTi_{1-x}O_2$ (M = W and Nb) samples and their respective fast Fourier transforms (FFT) related to the regions illustrated in (a) $Nb_{0.27}Ti_{0.73}O_2$ and (b) $W_{0.29}Ti_{0.71}O_2$.

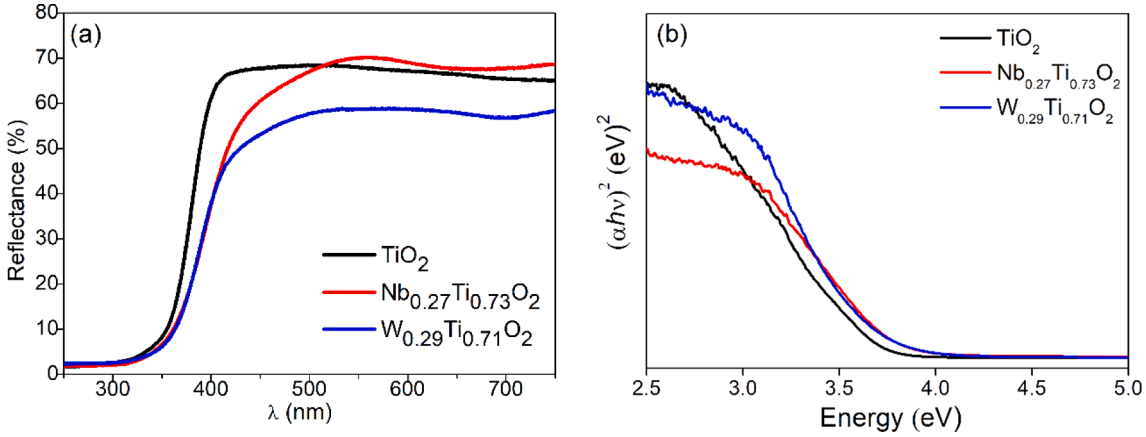

Fig. 6. (a) Representative diffuse reflectance spectra and (b) absorbance spectra of the TiO_2, $Nb_{0.27}Ti_{0.73}O_2$ and $W_{0.29}Ti_{0.71}O_2$ samples obtained from the Kulbelka-Munk equation.

peaks, as shown in Table 1. It was possible to observe a significantly high relative atomic percentage for the $Nb_{0.02}Ti_{0.98}O_2$ ($Ti^{+3}/Ti^{+4} = 0.03$) and $Nb_{0.27}Ti_{0.73}O_2$ ($Ti^{+3}/Ti^{+4} = 0.07$) samples compared to the pristine one, TiO_2 ($Ti^{+3}/Ti^{+4} = 0.02$), where the greater presence of Ti^{+3} for a higher Nb content indicated that some Ti^{4+} ions are reduced to Ti^{3+} ions, compensating additional positive charges associated with the presence of Nb^{5+} ions [3]. For the $W_xTi_{1-x}O_2$ samples, high relative atomic percentages of Ti^{+3}/Ti^{+4} were also observed in comparison with the pristine sample, but with no difference related to different amounts of dopant ($W_{0.03}Ti_{0.97}O_2$ and $W_{0.29}Ti_{0.71}O_2$). It was expected that the greater presence of W^{6+} or W^{4+} ions would induce a higher Ti^{4+} to Ti^{3+} reduction in order to compensate the additional positive charges. In this way, the XPS results for the $W_{0.29}Ti_{0.73}O_2$ samples (Fig. 7) indicates the presence of WO_x ions on the TiO_2 surface, as observed by Epifani et al [10].

To analyze the photocatalytic activity under ultraviolet (UV) irradiation, experiments were performed for the photodegradation of Methylene Blue (MB) and Rhodamine B dyes (RhB). The photooxidation curves of the MB and RhB dyes catalyzed by the studied samples (Fig. 10a and b) reveal that the Nb and W doped samples resulted in removal of the organic pollutants (i.e. MB and RhB dyes) used as a probe.

Table 2 exhibits the reaction rate constants (k) for the MB and RhB dye degradation obtained from the pseudo first-order model for the $M_xTi_{1-x}O_2$ (M = Nb and W) samples. Since the aim of this study was to evaluate the ozone-sensing properties and the photocatalytic performance of $M_xTi_{1-x}O_2$ (M = Nb and W) samples, which could be related to the surface area (SA), we obtained specific surface area values (SSA) through the BET method, also presented in Table 2. Despite the difference in their morphology (Fig. 3), there are no significant changes between the samples with respect to SSA values, except for $W_{0.03}Ti_{0.97}O_2$.

From the results in Table 2, it can be observed that all samples exhibited increased photocatalytic activity for the MB dye compared to the pure TiO_2, being the samples with higher dopant content ($Nb_{0.27}Ti_{0.73}O_2$ and $W_{0.29}Ti_{0.71}O_2$ samples) the ones that presented greater photocatalytic activity. On the other hand, $Nb_{0.27}Ti_{0.73}O_2$ and $W_{0.29}Ti_{0.71}O_2$ presented a worse photocatalytic activity for the RhB dye than the TiO_2 sample. Concerning the samples with lower dopant content, $W_{0.03}Ti_{0.97}O_2$ and mainly $Nb_{0.02}Ti_{0.98}O_2$ showed an improvement

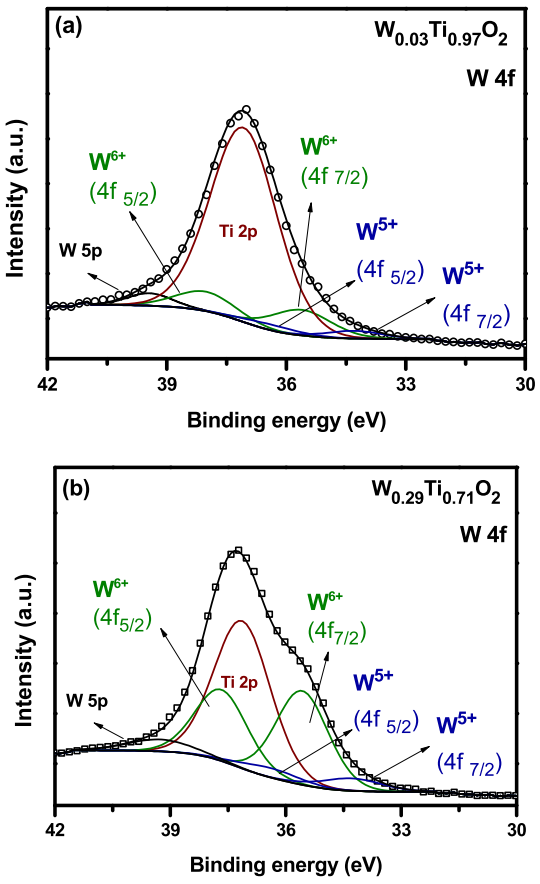

Fig. 7. HR W 4f XPS spectra of the $M_xTi_{1-x}O_2$ (M = W) samples: (a) $W_{0.03}Ti_{0.97}O_2$ and (b) $W_{0.29}Ti_{0.71}O_2$.

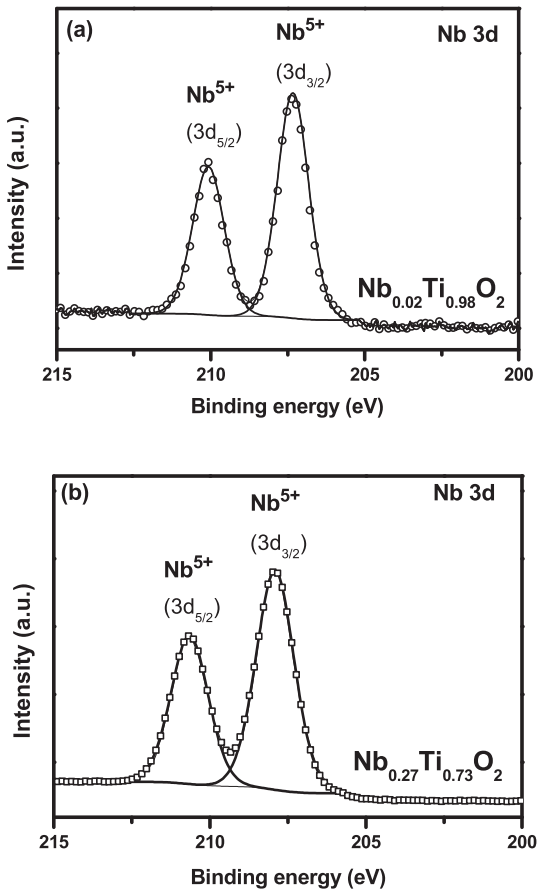

Fig. 8. HR Nb 3d XPS spectra of the $M_xTi_{1-x}O_2$ (M = Nb) samples: (a) $Nb_{0.02}Ti_{0.98}O_2$ and (b) $Nb_{0.27}Ti_{0.73}O_2$ samples.

in the photooxidation compared to the TiO_2 sample.

The enhancement of the as-studied $M_xTi_{1-x}O_2$ (M = W and Nb) samples can be explained by the surface interaction between the photocatalytic activity and the MB dye, which has a cationic characteristic, and the presence of metal ions in the structure, which consequently induces a change in the surface characteristic of the nanostructures [8,10,44]. On the other hand, the photocatalytic activity for the RhB dye appears to be strictly related to the electronic characteristics of the samples, whose higher activity could be explained by the structural defects observed in the Raman and XPS results. Nevertheless, the lower activity during the RhB photodegradation for higher amounts of dopant could be attributed to the increase in such structural defects with the increase of Nb and W, which was also confirmed by the Raman measurements. In fact, the high dopant density might generate some trapping for the charge carriers [7]. When studying $W_xTi_{1-x}O_2$ samples, Sathasivam et al. demonstrated that the degradation of the reassuring dye changed according to the W doping levels in TiO_2 films, where excess dopants can also be detrimental, leading to a worse photocatalytic activity for higher W amounts [7]. According to the authors, the carrier mobility was diminished with the increase of the dopant amounts, with W^{4+} ions acting as scattering sites for the charge carriers [7]. The presence of W^{m+} ions was observed in the XPS results.

Thus, the presence of W and Nb as dopant clearly induces a change in the surface characteristics, favoring the photodegradation of cationic dyes which does not occur for the RhB dye, whose photocatalytic mechanism appears to be strictly related to carrier charges, as already mentioned.

Electrical measurements were used to investigate the O_3 gas-sensing properties of the studied samples. Initially, we evaluated their optimum operating temperature in the range of 100–300 °C under exposure to 20 ppb of O_3 gas for 30 s. Nevertheless, for the pristine TiO_2 and $Nb_xTi_{1-x}O_2$ samples, no sensitivity towards O_3 was observed. Concerning the $W_xTi_{1-x}O_2$ samples, only the $W_{0.29}Ti_{0.71}O_2$ sample presented sensitivity towards O_3 gas in the levels studied. These results make clear that the gas-sensing activity is not only attributed to SSA or structural defects.

As it can be seen in Fig. 11, the $W_{0.29}Ti_{0.71}O_2$ sample presented sensitivity towards O_3 gas at a relatively low temperature, i.e., 100 °C, with a maximum response of 9. It is worth mentioning that the chemiresistor based on MOXs typically works in the temperature range of 150–400 °C [49,50]. Therefore, the results reported herein demonstrate that the insertion of tungsten into the TiO_2 matrix is capable of forming a sensing structure with ozone detection capabilities.

Based on the results above, the gas-sensing measurements were carried out by exposing the $W_{0.29}Ti_{0.71}O_2$ sample to different ozone concentrations (12 to 94 ppb) at a constant working temperature of 100 °C. Fig. 12 shows that the sample was sensitive to all ozone levels tested, also exhibiting total recovery after each cycle. The sensor response increased as a function of the ozone concentration, reaching a maximum response value of 30 at 94 ppb. After several exposure cycles,

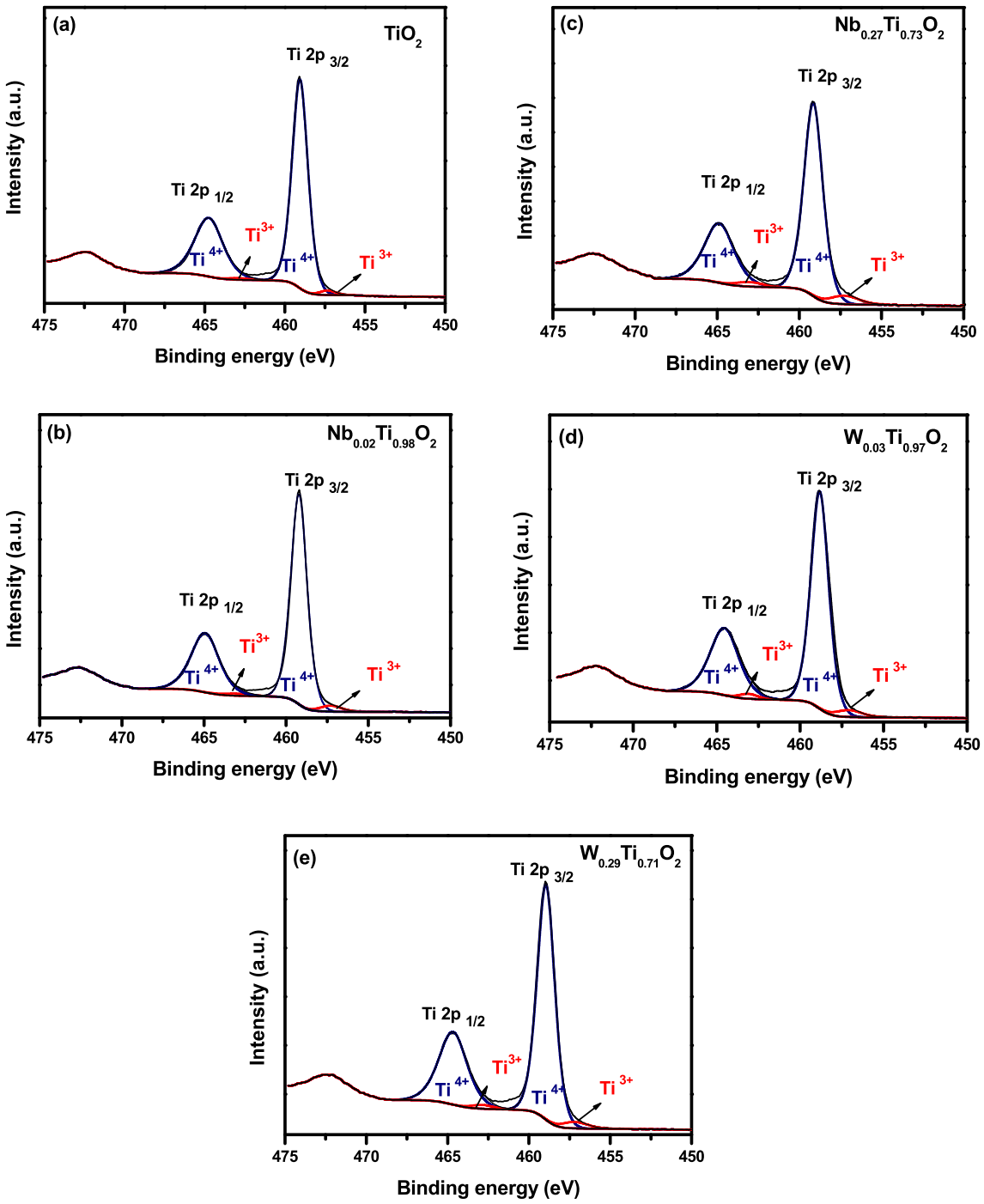

Fig. 9. HR 2p Ti XPS spectra of (a) TiO_2, (b) $Nb_{0.02}Ti_{0.98}O_2$, (c) $Nb_{0.27}Ti_{0.73}O_2$, (d) $W_{0.03}Ti_{0.97}O_2$ and (e) $W_{0.29}Ti_{0.71}O_2$ samples.

Table 1
Spectral fitting parameters for the relative atomic percentages (Ti^{+3}/Ti^{+4}) related to $2p_{3/2}$ transition for the titanium (Ti):

	Ti 2p 3/2				
	Ti^{3+}		Ti^{4+}		
Sample	%Area	BE, eV	%Area	BE, eV	Ti^{+3}/Ti^{+4}
TiO_2	1.3	457.3	65.3	459.1	0.02
$Nb_{0.02}Ti_{0.98}O_2$	2.2	457.2	64.4	459.2	0.03
$Nb_{0.27}Ti_{0.73}O_2$	4.1	457.2	63.6	459.1	0.07
$W_{0.03}Ti_{0.97}O_2$	2.5	457.1	64.2	458.9	0.04
$W_{0.29}Ti_{0.71}O_2$	2.8	457.1	63.9	458.8	0.04

it was possible to observe that the $W_{0.29}Ti_{0.71}O_2$ sensor could still detect low ozone concentration, indicating good reversibility and stability. Regarding response and recovery times, such sample presented a rapid detection of approximately 25 s (at 12 ppb of O_3), even after consecutive exposure cycles at higher O_3 levels, and a recovery time of 1.5 min.

As abovementioned, the $W_{0.29}Ti_{0.71}O_2$ sample detected from 12 to 94 ppb of O_3, thus demonstrating good range of detection which is considered to be essential for practical applications [51,52]. The toxicity levels of ozone gas allowed for humans can be influenced by a variety of parameters (e.g., preexisting disease, age and genetic factors) [51]. However, various organizations worldwide recommend a limit of O_3 levels in the air in the range of 50 to 120 ppb for an exposure time of 1–8 h. [52]

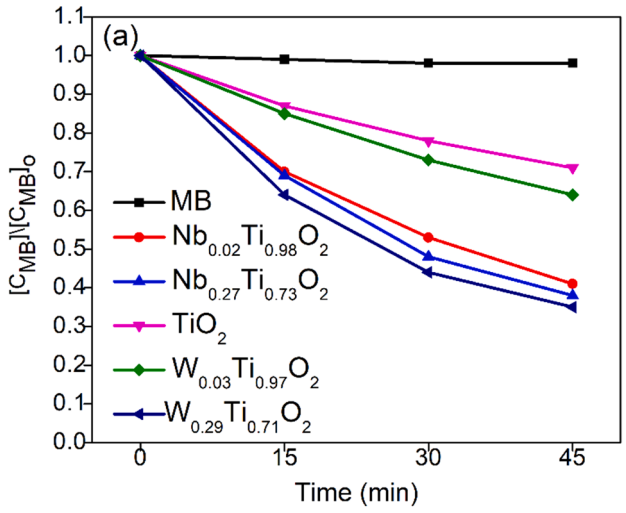

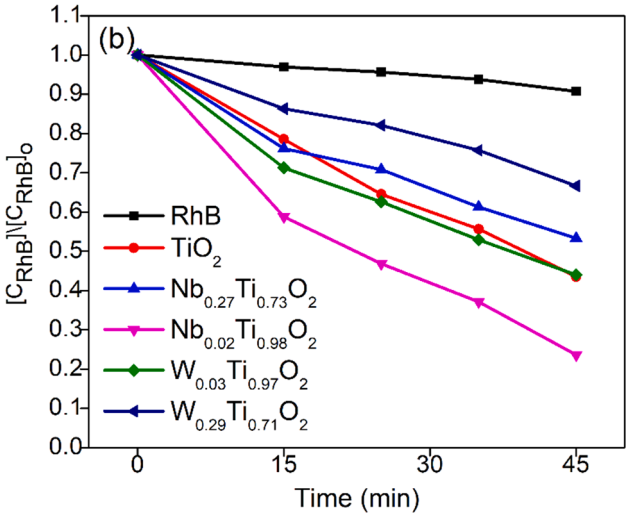

Fig. 10. Photodegradation curves for the (a) MB and (b) RhB dyes under ultraviolet light (UV) for the $M_xTi_{1-x}O_2$ (M = W and Nb) samples.

Table 2
First-order rate constants (k) for MB and RhB dye photodegradation reaction under UV irradiation, specific surface area (SSA) and rate constants per unit area (k/SA) of $M_xTi_{1-x}O_2$ (M = W and Nb) samples.

Samples	K_{MB} (min^{-1})	K_{RhB} (min^{-1})	SSA (m^2/g)	K_{MB}/SA	K_{RhB}/SA
TiO_2	0.00757	0.01843	63	1.2x10^{-4}	2.9x10^{-4}
$Nb_{0.02}Ti_{0.98}O_2$	0.01896	0.02849	51	3.7x10^{-4}	5.6x10^{-4}
$Nb_{0.27}Ti_{0.73}O_2$	0.02055	0.01365	50	4.1x10^{-4}	2.7x10^{-4}
$W_{0.03}Ti_{0.97}O_2$	0.00995	0.01827	36	2.7x10^{-4}	5.0x10^{-4}
$W_{0.29}Ti_{0.71}O_2$	0.02343	0.00879	52	4.5x10^{-4}	1.6x10^{-4}

To gain further insight into the possible practical application of the W-doped sample as an ozone-sensing layer, its long-term stability was also evaluated. For this purpose, for approximately 1 year the sample was exposed to 20 ppb of O_3 at an operating temperature of 100 °C. The obtained results are shown in Fig. 13, where it is possible to note that after a long period of time the sample still detected low ozone concentration, demonstrating the great potential of $W_{0.29}Ti_{0.71}O_2$ materials as a gas-sensing layer for the detection of sub-ppm ozone levels.

As a matter of fact, there are relatively few studies and reports in the literature regarding volatile hazardous gas sensors based on TiO_2. The improvement of the sensing performance of MOX-based gas sensors

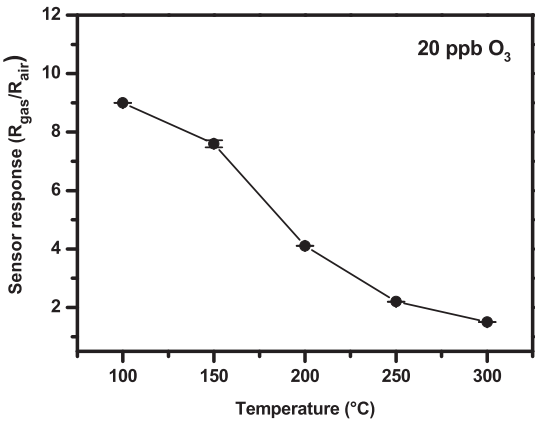

Fig. 11. Ozone gas-sensing response of the $W_{0.29}Ti_{0.71}O_2$ sample towards 20 ppb of O_3 at various operating temperature.

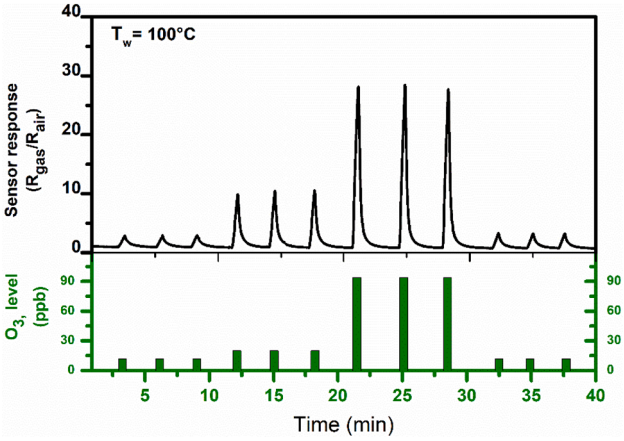

Fig. 12. Ozone gas-sensing response of the $W_{0.29}Ti_{0.71}O_2$ sample exposed to different O_3 levels (12, 20 and 94 ppb) at an working temperature (T_w) of 100 °C.

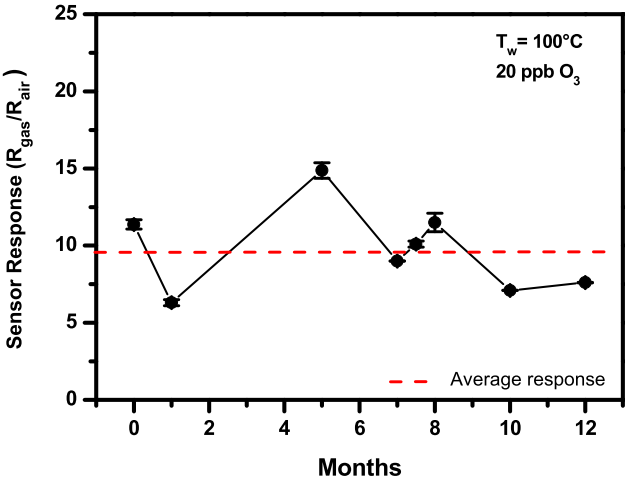

Fig. 13. Long-term stability of the $W_{0.29}Ti_{0.71}O_2$ sample upon an exposure to 20 ppb of ozone for approximately 1 year.

arises from a synergistic combination of multiple factors. Herein, the presence of oxygen vacancies or defect concentration on the surface of the samples (observed by XPS) might facilitate the chemisorption process, which could contribute to an improved the gas-sensing performance of the material [6,36]. The Raman results also pointed to the presence of structural defects for all studied samples, such as oxygen vacancies. Nevertheless, the improvement of the detection capability cannot be substantiated only from the viewpoint of oxygen vacancies or defect concentration on the surface, since we did not find sensitivity towards O_3 gas for the pristine TiO_2 and $Nb_xTi_{1-x}O_2$ samples. The morphological characteristics, and consequently the surface area, are also aspects that can be attributed to sensor performance, yet they cannot explain the difference in results obtained for the studied samples. Some works report that the surface modification of TiO_2 anatase could improve the chemiresistive sensor response [8,10,13], as demonstrated by Epifani et al. who reported an improvement of 3 orders of magnitude in the ethanol sensing properties of TiO_2 surface modified with WO_x compared to pure TiO_2 [10]. For the $W_{0.29}Ti_{0.71}O_2$ sample, the sensitivity towards O_3 gas could be explained by the presence of WO_x on the surface of TiO_2 particles, as suggested by the XPS results. On the other hand, it is well known that for being typical n-type semiconductors the working principle of TiO_2-based gas sensors is based on the conductance change mechanism due to the adsorption/desorption process of oxidizing and reducing gases [1,36]. In this way, the electronic characteristics of the studied samples, such as the conductance change induced by the introduction of different types and quantities of metal ions, clearly play an important role in the sensor performance.

It is important to highlight that $W_{0.29}Ti_{0.71}O_2$ nanostructures exhibit remarkable O_3 sensing properties for practical applications. Among them, we can cite their relatively low operating temperature, good range of detection, good sensor response, stability and reversibility towards O_3 gas sensor.

4. Conclusion

In summary, we have employed a simple and environmentally-friendly method to obtain doped TiO_2 anatase nanostructures ($M_xTi_{1-x}O_2$ (M = W and Nb)). Changes in the morphology of the studied samples were observed as a function of dopant content, yet without a significant change in the band-gap due to the presence of W or Nb. The $M_xTi_{1-x}O_2$ (M = W and Nb) samples presented favorable photocatalytic performance when employed for the degradation of the MB and RhB dyes, indicating a selective performance. Additionally, it was found that despite their surface characteristics, their electronic characteristics related to different types and quantities of metal ions played an important role in their photocatalytic activity and gas-sensing performance. For the TiO_2 sample containing a higher amount of W ($W_{0.29}Ti_{0.71}O_2$), the presence of surface characteristics related to WO_x species revealed a promising gas-sensing property towards O_3 gas, especially when at low working temperatures.

CRediT authorship contribution statement

Emerson Santos: Investigation, Methodology, Data curation, Writing – original draft. **Ariadne C. Catto:** Investigation, Methodology, Writing – review & editing. **Allan F. Peterline:** Investigation, Methodology, Writing – review & editing. **Waldir Avansi Jr:** Conceptualization, Investigation, Methodology, Data curation, Writing – review & editing, Supervision, Project administration.

Declaration of Competing Interest

The authors declare that they have no known competing financial interests or personal relationships that could have appeared to influence the work reported in this paper.

Acknowledgements

The authors gratefully acknowledge the financial support of the Brazilian research funding agencies FAPESP (under grant numbers 2013/17639-4, 2013/07296-2, 17/18649-4, 2017/12437-5 and 2018/18208-0), CNPq (311463/2017-7, 426511/2018-2 and 431586/2018-7) and CAPES (Financial Code 001). Brazilian Metallurgy and Mining Company (CBMM) is acknowledged for the Niobium samples supply. Also, we would you like to acknowledge to Embrapa Instrumentation for electron microscopy, Raman and BET facilities. Transmission electron microscopy (TEM) and X-ray photoelectron spectroscopy (XPS - 20607) were performed at the LME/LNNano/CNPEM. The electrodes used for the gas-sensing experiments were fabricated in the Laboratory of Microfabrication at the LNNano/CNPEM (Project LMF-18580).

References

[1] D. Nunes, A. Pimentel, A. Gonçalves, S. Pereira, R. Branquinho, P. Barquinha, E. Fortunato, R. Martins, Metal oxide nanostructures for sensor applications, Semicond. Sci. Technol. 34 (4) (2019).
[2] D.S. Bhachu, S. Sathasivam, G. Sankar, D.O. Scanlon, G. Cibin, C.J. Carmalt, I. P. Parkin, G.W. Watson, S.M. Bawaked, A.Y. Obaid, S. Al-Thabaiti, S.N. Basahel, Solution processing route to multifunctional titania thin films: highly conductive and photcatalytically active Nb:TiO_2, Adv. Funct. Mater. 24 (2014) 5075–5085.
[3] Q. Sun, D. Cortie, S. Zhang, T.J. Frankcombe, G. She, J. Gao, L.R. Sheppard, W. Hu, H. Chen, S. Zhuo, D. Chen, R.L. Withers, G. McIntyre, D. Yu, W. Shi, Y. Liu, The formation of defect-pairs for highly efficient visible-light catalysts, Adv. Mater. 29 (11) (2017).
[4] S.m. Chang, W.s. Liu, The roles of surface-doped metal ions (V, Mn, Fe, Cu, Ce, and W) in the interfacial behavior of TiO_2 photocatalysts, Applied Catalysis B-Environmental, 156 (2014) 466-475.
[5] S.N.R. Inturi, T. Boningari, M. Suidan, P.G. Smirniotis, Visible-light-induced photodegradation of gas phase acetonitrile using aerosol-made transition metal (V, Cr, Fe Co, Mn, Mo, Ni, Cu, Y, Ce, and Zr) doped TiO2, Appl. Catal. B-Environ. 144 (2014) 333–342.
[6] S. Mokrane-Soualah, A.S. Gago, A. Habrioux, N. Alonso-Vante, Mixed-oxide $Ti_{1-x}W_xO_2$ as support for (photo)-electrochemical processes, Appl. Catal. B-Environ. 147 (2014) 756–763.
[7] S. Sathasivam, D.S. Bhachu, Y. Lu, N. Chadwick, S.A. Althabaiti, A.O. Alyoubi, S. N. Basahel, C.J. Carmalt, I.P. Parkin, Tungsten doped TiO_2 with enhanced photocatalytic and optoelectrical properties via aerosol assisted chemical vapor deposition, Sci. Rep. 5 (1) (2015).
[8] M. Epifani, R. Diaz, C. Force, E. Comini, T. Andreu, R.R. Zamani, J. Arbiol, P. Siciliano, G. Faglia, J.R. Morante, Colloidal counterpart of the TiO_2-supported V_2O_5 system: a case study of oxide-on-oxide deposition by wet chemical techniques. synthesis, vanadium speciation, and gas-sensing enhancement, J. Phys. Chem. C 117 (2013) 20697–20705.
[9] M. Epifani, E. Comini, R. Diaz, C. Force, P. Siciliano, G. Faglia, TiO_2 colloidal nanocrystals surface modification by V_2O_5 species: Investigation by Ti-47, Ti-49 MAS-NMR and $_H$2, CO and N_O2 sensing properties, Appl. Surf. Sci. 351 (2015) 1169–1173.
[10] M. Epifani, R. Díaz, C. Force, E. Comini, M. Manzanares, T. Andreu, A. Genç, J. Arbiol, P. Siciliano, G. Faglia, J.R. Morante, Surface modification of TiO 2 nanocrystals by WO x coating or wrapping: solvothermal synthesis and enhanced surface chemistry, ACS Appl. Mater. Interfaces 7 (12) (2015) 6898–6908.
[11] S.m. Chang, W.s. Liu, Surface doping is more beneficial than bulk doping to the photocatalytic activity of vanadium-doped TiO_2, Applied Catalysis B-Environmental, 101 (2011) 333-342.
[12] Q. Wu, Q. Zheng, R. van de Krol, Creating oxygen vacancies as a novel strategy to form tetrahedrally coordinated Ti^{4+} in Fe/TiO_2 nanoparticles, J. Phys. Chem. C 116 (2012) 7219–7226.
[13] W. Avansi, A.C. Catto, L.F. da Silva, T. Fiorido, S. Bernardini, V.R. Mastelaro, K. Aguir, R. Arenal, One-dimensional V_2O_5/TiO_2 heterostructures for chemiresistive ozone sensors, ACS Appl. Nano Mater. 2 (8) (2019) 4756–4764.
[14] I.A. de Castro, W. Avansi, C. Ribeiro, WO_3/TiO_2 heterostructures tailored by the oriented attachment mechanism: insights from their photocatalytic properties, CrystEngComm 16 (2014) 1514–1524.
[15] M.R. Hoffmann, S.T. Martin, W.Y. Choi, D.W. Bahnemann, environmental applications of semiconductor photocatalysis, Chem. Rev. 95 (1995) 69–96.
[16] G.R. Bamwenda, T. Uesigi, Y. Abe, K. Sayama, H. Arakawa, The photocatalytic oxidation of water to O_2 over pure CeO_2, WO_3, and TiO_2 using Fe^{3+} and Ce^{4+} as electron acceptors, Appl. Catal. a-General 205 (2001) 117–128.
[17] O.F. Lopes, E.C. Paris, C. Ribeiro, Synthesis of Nb_2O_5 nanoparticles through the oxidant peroxide method applied to organic pollutant photodegradation: a mechanistic study, Appl. Catal. B-Environ. 144 (2014) 800–808.
[18] C.-F. Yu, S.-J. Sun, J.-M. Chen, Magnetic and electrical properties of TiO_2: Nb thin films, Appl. Surf. Sci. 292 (2014) 773–776.
[19] K. Chen, J. Li, W. Wang, Y. Zhang, X. Wang, H. Su, The preparation of vanadium-doped TiO_2 montmorillonite nanocomposites and the photodegradation of sulforhodamine B under visible light irradiation, Appl. Surf. Sci. 257 (2011) 7276–7285.

[20] M. Khan, W. Cao, N. Chen, Z. Usman, D.F. Khan, A.M. Toufiq, M.A. Khaskheli, Influence of tungsten doping concentration on the electronic and optical properties of anatase TiO_2, Curr. Appl Phys. 13 (2013) 1376–1382.

[21] L.F. da Silva, W. Avansi, A.C. Catto, J.E.F.S. Rodrigues, M.I.B. Bernardi, V. R. Mastelaro, The role of Nb addition in TiO_2 Nanoparticles: phase transition and photocatalytic properties, Phys. Status Solidi A 215 (21) (2018) 1800321.

[22] W. Avansi, R. Arenal, V.R. de Mendonca, C. Ribeiro, E. Longo, Vanadium-doped TiO_2 anatase nanostructures: the role of V in solid solution formation and its effect on the optical properties, CrystEngComm 16 (2014) 5021–5027.

[23] J. Yue, C. Suchomski, P. Voepel, R. Ellinghaus, M. Rohnke, T. Leichtweiss, M. T. Elm, B.M. Smarsly, Mesoporous niobium-doped titanium dioxide films from the assembly of crystalline nanoparticles: study on the relationship between the band structure, conductivity and charge storage mechanism, J. Mater. Chem. A 5 (2017) 1978–1988.

[24] X. Kang, S. Liu, Z. Dai, Y. He, X. Song, Z. Tan, Titanium dioxide: from engineering to applications, Catalysts 9 (2019) 2–32.

[25] M. Epifani, R. Diaz, C. Force, E. Comini, M. Manzanares, T. Andreu, A. Genc, J. Arbiol, P. Siciliano, G. Faglia, J.R. Morante, Surface modification of TiO_2 nanocrystals by WO_x coating or wrapping: solvothermal synthesis and enhanced surface chemistry, ACS Appl. Mater. Interfaces 7 (2015) 6898–6908.

[26] A.J. Gardecka, G.K.L. Goh, G. Sankar, I.P. Parkin, On the nature of niobium substitution in niobium doped titania fhin films by AACVD and its impact on electrical and optical properties, J. Mater. Chem. A 7 (2015) 17755–17762.

[27] L. Sheppard, T. Bak, J. Nowotny, C.C. Sorrell, S. Kumar, A.R. Gerson, M.C. Barnes, C. Ball, Effect of niobium on the structure of titanium dioxide thin films, Thin Solid Films 510 (1-2) (2006) 119–124.

[28] A.C. Catto, L.F.d. Silva, M.I.B. Bernardi, S. Bernardini, K. Aguir, E. Longo, V. R. Mastelaro, Local Structure and Surface Properties of $Co_xZn_{1-x}O$ Thin Films for Ozone Gas Sensing, ACS Appl. Mater. Interfaces 8 (39) (2016) 26066–26072.

[29] I.A. Yang, O. Holz, A. Jorres, H. Magnussen, S.J. Barton, S. Rodriguez, J. A. Cakebread, J.W. Holloway, S.T. Holgate, Association of tumor necrosis factor-alpha polymorphisms and ozone-induced change in lung function, Am. J. Respir. Crit. Care Med. 171 (2005) 171–176.

[30] O. Holz, R.A. Jörres, P. Timm, M. Mücke, K. Richter, S. Koschyk, H. Magnussen, Ozone-induced airway inflammatory changes differ between individuals and are reproducible, Am. J. Respir. Crit. Care Med. 159 (3) (1999) 776–784.

[31] W.J. Gauderman, G.F. Gilliland, H. Vora, E. Avol, D. Stram, R. McConnell, D. Thomas, F. Lurmann, H.G. Margolis, E.B. Rappaport, K. Berhane, J.M. Peters, Association between air pollution and lung function growth in Southern California children - results from a second cohort, Am. J. Respir. Crit. Care Med. 166 (2002) 76–84.

[32] R. Jorres, D. Nowak, H. Magnussen, P. Speckin, S. Koschyk, The effect of ozone exposure on allergen responsiveness in subjects with asthma or rhinitis, Am. J. Respir. Crit. Care Med. 153 (1996) 56–64.

[33] S. Vallejos, V. Khatko, K. Aguir, K.A. Ngo, J. Calderer, I. Gracia, C. Cane, E. Llobet, X. Correig, Ozone monitoring by micro-machined sensors with WO_3 sensing films, Sens. Actuat. B-Chem. 126 (2007) 573–578.

[34] W. Belkacem, A. Labidi, J. Guerin, N. Mliki, K. Aguir, Cobalt nanograins effect on the ozone detection by WO_3 sensors, Sens. Actuat. B-Chem. 132 (2008) 196–201.

[35] G. Korotcenkov, I. Blinov, M. Ivanov, J.R. Stetter, Ozone sensors on the base of SnO2 films deposited by spray pyrolysis, Sens. Actuat. B-Chem. 120 (2007) 679–686.

[36] L.F. da Silva, A.C. Catto, W. Avansi, L.S. Cavalcante, J. Andres, K. Aguir, V. R. Mastelaro, E. Longo, A novel ozone gas sensor based on one-dimensional (1D) alpha-Ag_2WO_4 nanostructures, Nanoscale 6 (2014) 4058–4062.

[37] A.C. Catto, T. Fiorido, É.L.S. Souza, W. Avansi, J. Andres, K. Aguir, E. Longo, L. S. Cavalcante, L.F. da Silva, Improving the ozone gas-sensing properties of $CuWO_4$ nanoparticles, J. Alloy. Compd. 748 (2018) 411–417.

[38] J.-Y. Piquemal, E. Briot, J.-M. Brégeault, Preparation of materials in the presence of hydrogen peroxide: from discrete or “zero-dimensional” objects to bulk materials, Dalton Trans. 42 (1) (2013) 29–45.

[39] W. Avansi Jr., C. Ribeiro, E.R. Leite, V.R. Mastelaro, Vanadium pentoxide nanostructures: an effective control of morphology and crystal structure in hydrothermal conditions, Cryst. Growth Des. 9 (8) (2009) 3626–3631.

[40] V.R. de Mendonça, O.F. Lopes, W. Avansi, R. Arenal, C. Ribeiro, Insights into formation of anatase TiO_2 nanoparticles from peroxo titanium complex degradation under microwave-assisted hydrothermal treatment, Ceram. Int. 45 (17) (2019) 22998–23006.

[41] C. Ribeiro, C. Barrado, E. deCamargo, E. Longo, E. Leite, Phase transformation in titania nanocrystals by the oriented attachment mechanism: the role of the pH value, Chem.-a Eur. J. 15 (9) (2009) 2217–2222.

[42] K. Suzuki, K. Kijima, Optical band gap of barium titanate nanoparticles prepared by RF-plasma chemical vapor deposition, Japanese Journal of Applied Physics Part 1-Regular Papers Brief Communications & Review Papers, 44 (2005) 2081-2082.

[43] D.L. Wood, J. Tauc, weak absorption tails in amorphous semiconductors, Phys. Rev. B 5 (8) (1972) 3144–3151.

[44] W. Avansi, V.R. de Mendonça, O.F. Lopes, C. Ribeiro, Vanadium pentoxide 1-D nanostructures applied to dye removal from aqueous systems by coupling adsorption and visible-light photodegradation, RSC Adv. 5 (16) (2015) 12000–12006.

[45] A.C. Catto, M.M. Ferrer, O.F. Lopes, V.R. Mastelaro, J. Andrés, L.F. da Silva, E. Longo, W. Avansi, The role of counter-ions in crystal morphology, surface structure and photocatalytic activity of ZnO crystals grown onto a substrate, Appl. Surf. Sci. 529 (2020) 147057.

[46] F. Fresno, D. Tudela, J.M. Coronado, M. Fernández-García, A.B. Hungría, J. Soria, Influence of Sn^{4+} on the structural and electronic properties of $Ti_{1-x}Sn_xO_2$ nanoparticles used as photocatalysts, PCCP 8 (20) (2006) 2421–2430.

[47] M. Vasilopoulou, A. Soultati, D.G. Georgiadou, T. Stergiopoulos, L.C. Palilis, S. Kennou, N.A. Stathopoulos, D. Davazoglou, P. Argitis, Hydrogenated under-stoichiometric tungsten oxide anode interlayers for efficient and stable organic photovoltaics, J. Mater. Chem. A 2 (6) (2014) 1738–1749.

[48] A.M. Smith, M.G. Kast, B.A. Nail, S. Aloni, S.W. Boettcher, A planar-defect-driven growth mechanism of oxygen deficient tungsten oxide nanowires, J. Mater. Chem. A 2 (17) (2014) 6121–6129.

[49] G. Korotcenkov, Metal oxides for solid-state gas sensors: What determines our choice? Mater. Sci. Eng. B-Solid State Mater. Adv. Technol. 139 (1) (2007) 1–23.

[50] A.C. Catto, M.C. Oliveira, R.A.P. Ribeiro, W. Avansi, L.F. da Silva, E. Longo, Hematite rhombuses for chemirestive ozone sensors: Experimental and theoretical approaches, Appl. Surf. Sci. 563 (2021) 150209.

[51] C.J. Weschler, Ozone’s impact on public health: contributions from indoor exposures to ozone and products of ozone-initiated chemistry, Environ. Health Perspect. 114 (2006) 7.

[52] T.S.H. Salonen, L. Morawska, Human exposure to ozone in school and office indoor environments, Environ. Int. 119 (2018) 11.